


## Search for a possible flexible-to-rigid transition in models of phase change materials

M. Micoulaut<sup>1,\*</sup> and H. Flores-Ruiz<sup>2</sup>

<sup>1</sup>*Sorbonne Université, Laboratoire de Physique Théorique de la Matière Condensée, CNRS UMR 7600, 4 Place Jussieu, 75252 Paris Cedex 05, France*

<sup>2</sup>*Departamento de Ciencias Naturales y Exactas, CUValles, Universidad de Guadalajara, Carr. Guadalajara-Ameca km 45.5, 46600, Ameca, Jalisco, México*

 (Received 7 December 2020; revised 1 April 2021; accepted 5 April 2021; published 19 April 2021)

Structural models of the prototypical phase change material Ge-Sb-Te are generated from first-principles molecular dynamics simulations with a particular attention to the  $\text{Ge}_x\text{Sb}_x\text{Te}_{100-2x}$  join. Constraint counting algorithms permit us to analyze the obtained amorphous networks within the framework of topological constraint (rigidity) theory. A flexible-to-rigid transition is found at  $x \simeq 8.5\%$  which satisfies the Maxwell isostatic criterion and is characterized by an important topological disorder with large amounts of mixed geometries and miscoordinations. The angular constraint count furthermore leads to the identification of tetrahedral Ge sites whose population decreases with growing Ge/Sb content and is about 55% for  $\text{Ge}_2\text{Sb}_2\text{Te}_5$ . Sb sites change from a dominant pyramidal geometry typical of Group V chalcogenides to a defect octahedral one which is reminiscent of the crystalline polymorph of  $\text{Ge}_2\text{Sb}_2\text{Te}_5$ .

DOI: [10.1103/PhysRevB.103.134206](https://doi.org/10.1103/PhysRevB.103.134206)

### I. INTRODUCTION

Amorphous chalcogenides represent an attractive class of materials with promising applications in optoelectronics, and most of the properties can be changed continuously to be optimized with chemical composition [1]. These physical, chemical, or electronic properties result essentially from the deep modification of the network characteristics which evolve starting from a near one-dimensional (1D) chain structure typical of the base elements (S, Se, and Te) to a continuous three-dimensional (3D) network structure. Among such systems, amorphous tellurides appear to be attractive but also challenging materials given the increased crystallization tendency of elemental Te and the subsequent typical alloys. This dramatically reduces the glass-forming region (GFR) [2–4] when contrasted with corresponding, e.g., selenides (Fig. 1). Furthermore, tellurides appear to not fulfill the “ $8-\mathcal{N}$ ” rule that could predict network structures in, e.g., Ge-Sb-Te from fourfold coordinated Ge, threefold coordinated Sb, and twofold coordinated Te atoms [11,12]. Here,  $\mathcal{N}$  represents the number of valence electrons for a given chemical species. Instead, Te appears to have a coordination number  $r_{\text{Te}} \geq 2$  that also evolves with increasing temperature [13], and Ge is found in different geometries [14].

The glass structure of tellurides provides, therefore, a strong contrast to the other S- or Se-based chalcogenides which display (i) well-established coordination numbers both from theory and experiments [15], (ii) well-defined geometries entirely based on, e.g., tetrahedral (T) Ge and pyramidal (PYR) Group V atoms that serve to characterize the underlying network topology [16], (iii) extended GFRs [1], and

(iv) reduced crystallization tendencies [17]. Regarding the latter, the temperature dependence of transport properties (e.g., viscosity, diffusivity) plays obviously an important role in the enhanced nucleation and/or growth rates of crystalline polymorphs in Te-based liquids [18]. These unique properties are used to design phase-change materials able to switch on the nanosecond timescale between a crystalline and an amorphous phase with large optical or electrical contrast [19].

For such materials, it is certainly desirable to produce realistic structure models that could help in decoding properties and also producing *in silico* design of new compositions or applications. In this respect, topological constraint theory (TCT) or rigidity theory appears to be central for an increased understanding of the role of network topology on properties in the amorphous phase as well as locating compositions at which glass-forming tendency is promoted.

#### A. Rigidity transitions

In its initial mean-field version, TCT considers the molecular network as an analog of a mechanical truss made of bars (i.e., bonds) and nodes (i.e., atoms) for which a Maxwell mechanical stability analysis can be performed [20]. This approach can be cast into an elastic phase transition problem driven by the average coordination number  $\bar{r}$  which acts as an external parameter for the transition [21,22]. The latter transition is obtained between an elastically flexible underconstrained network to a stressed-rigid network that is overconstrained by radial and angular interactions. The *locus* of the transition is found when the average number of constraints per atom  $n_c = 3$ , the number of degrees of freedom per atom in 3D, corresponding to the well-known Maxwell isostatic criterion [23]. Experimentally, this transition has been detected in various glassy systems at the average

\*[mmi@lptmc.jussieu.fr](mailto:mmi@lptmc.jussieu.fr)

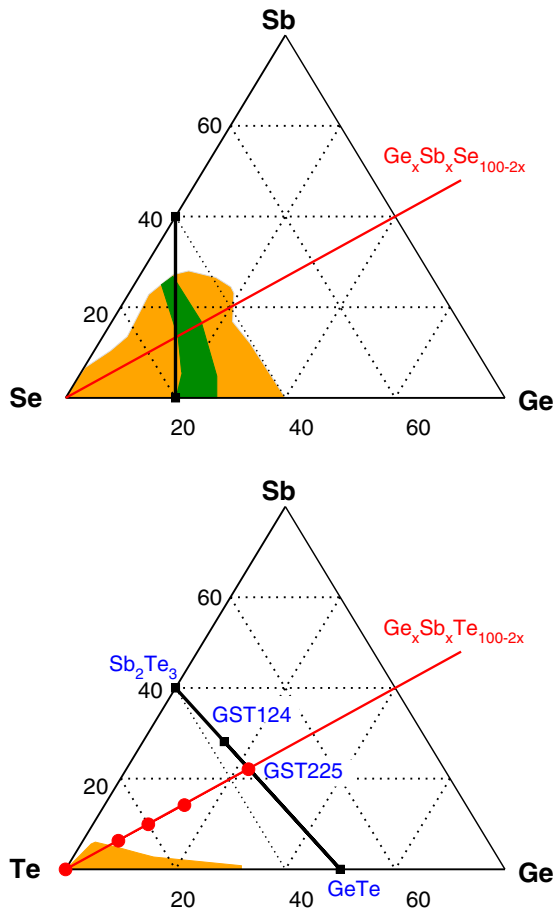


FIG. 1. Glass-forming region (orange) in Ge-Sb-Te (top [5–7]) and Ge-Sb-Te (bottom [8–10]) obtained from melt quench. In selenides, an intermediate phase develops (green [6]), and a possible flexible-to-rigid transition can be expected along the  $\text{Sb}_2\text{Te}_3$ - $\text{GeSe}_4$  join (black line). In Ge-Sb-Te, the present investigated compositions are found on the red line  $\text{Ge}_x\text{Sb}_x\text{Te}_{100-2x}$  (see text for details). The typical phase change materials are given in blue and are found on the  $\text{Sb}_2\text{Te}_3$ - $\text{GeTe}$  join.

coordination number of  $\bar{r}_c = 2.4$ , this condition being fulfilled exactly when all bond-stretching (BS) and bond-bending (BB) constraints are intact and no dangling bonds are present [24]. Given the generic character of the approach, such behaviors have been found in a variety of selenide and sulfide systems [25], independently of chemical composition and relying solely on  $\bar{r}$ . This is known in the literature as the isocoordinate rule that has been probed numerically [26] and experimentally [27].

More recent theoretical and experimental work has indicated that two transitions can occur and will separate the flexible and stressed-rigid phases by an intermediate phase (IP) [28] which results from a possible self-organization during glass transition to reduce energetically unfavorable configurations and maintains isostatically rigid but stress-free networks over a finite compositional interval [29–32]. The detection of this phase is realized from the measurement of a relaxation (nonreversing) enthalpy  $\Delta H_{nr}$  accessed from temperature-modulated differential scanning calorimetry experiments [33–35]. Across the compositions defining

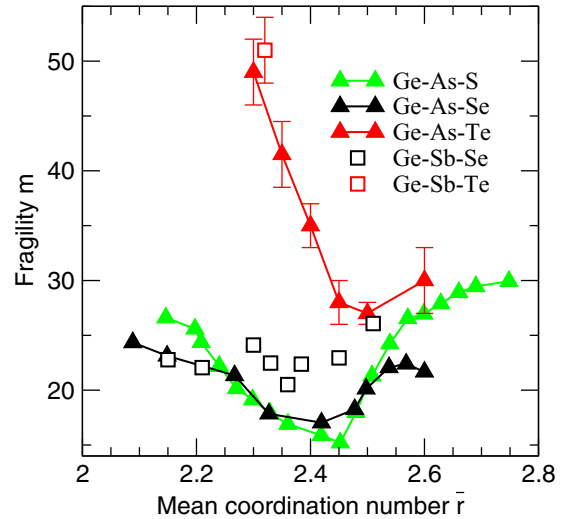


FIG. 2. Fragility of ternary chalcogenides of the same family Ge-As-X and Ge-Sb-X ( $X = \text{S}, \text{Se}, \text{or Te}$ ). Data from Ge-As-S [55], Ge-As-Se [39], Ge-As-Te [9], Ge-Sb-Se [6], and Ge-Sb-Te [9]. Note that, for convenience, all data are here represented as a function of the mean coordination number  $\bar{r}$  according to the 8- $\mathcal{N}$  rule, which is known not to be fully valid in tellurides.

the IP, this nonreversible enthalpy takes a minimal value, but other quantities also display anomalies and threshold behaviors as also detected from molecular dynamics (MDs) simulations [36–38]. For the  $\text{Ge}_x\text{As}_x\text{Se}_{100-2x}$  system [39], this composition range is reported as  $9.5\% < x < 17\%$  or  $2.28 < \bar{r} < 2.51$ , and different anomalies are evidenced such as minima in relaxation and thermal properties with composition or  $\bar{r}$ .

## B. Fingerprints of rigidity transitions in tellurides

We are only aware of a select number of systems where a direct measurement of  $\Delta H_{nr}$  has permitted one to identify flexible-to-rigid transitions and IPs in tellurides. IPs have been measured in different Group IV and Group V tellurides such as Ge-Si-Te [4,40], Ge-Te-In-Ag [41,42], Ge-Te-Cu [43], Ge-Te-In [44]. For other telluride materials, a useful means to detect onset of rigidity and IPs builds on the strong-fragile melt classification that measures the viscosity evolution  $\eta(T)$  with temperature and composition in stoichiometric glass-forming melts, alcohols, sugars, and organic polymers. From papers by Laughlin and Uhlmann [45] and Angell [46], the corresponding fragility index

$$m(x) = \left[ \frac{d \log_{10} \eta(x, T)}{dT_g(x)/T} \right]_{T=T_g(x)}, \quad (1)$$

displays nonmonotonic behavior with composition  $x$  or average coordination number  $\bar{r}$  for the case of nonstoichiometric glass-forming melts undergoing flexible-to-rigid transitions, as acknowledged [47] for the As-Ge-Se ternary, which shows a minimum in  $m(\bar{r})$  and in the associated activation energy for viscous flow or enthalpic relaxation near  $\bar{r} = 2.40$  (Fig. 2). More recent work on a large body of selenide and sulfide melts indicates that the fragility index  $m(x)$  takes on a rather low value of about 15 for concentrations belonging to

the IP where the enthalpic relaxation at the glass transition temperature is minuscule [39,48–51]. A theoretical link among enthalpic changes, fragility, and isostatic character of the glass network has been established from analytical models [52,53] and also confirmed quantitatively from molecular simulations [36,54].

In tellurides, given the increased crystallization tendency, only sparse data are available (Fig. 2). These reflect, indeed, a possibility of a flexible-to-rigid transition that might manifest by minimum in fragility for relaxation such as Ge-As-Te [9], which is found at a somewhat larger mean coordination number ( $\bar{r} \simeq 2.5$ ) than corresponding sulfides or selenides ( $\bar{r} \simeq 2.45$  [39,55]). An opposite shift is encountered for Si-Ge-Te [4] with a minimum found for  $m$  at  $\bar{r} = 2.34$ . In related binary glasses (e.g.,  $\text{Ge}_x\text{Te}_{100-x}$ ), a systematic investigation of  $m(x)$  has not been performed, but some data [56] indicate a decrease in the telluride-rich region down to  $\text{GeTe}_4$ , similarly to the corresponding sulfides [34] or selenides [48]. For materials displaying phase change properties such as Ge-Sb-Te, only two compositions have been investigated from this viewpoint, i.e.,  $\text{Ge}_{15}\text{Sb}_2\text{Te}_{83}$  ( $m = 51$  [9]),  $\text{Ge}_2\text{Sb}_2\text{Te}_5$  ( $m = 90$  [57] or  $m = 129$  [58]), and the detection of a possible flexible-to-rigid transition from fragility measurements is unfortunately excluded by the fast crystallization of the liquids.

### C. Glass formation in Ge-Sb-Te systems

It has been recognized that a network that is rigid but stress-free and that satisfies  $n_c = 3$  lies at a mechanical critical point that influences the glass-forming ability [25]. In fact, the presence of flexible modes in chalcogen-rich regions brings an additional increase to the heat of vitrification, whereas the absence of excess constraints prevents phase separation. The result is that glass formation at the rigidity transition composition should be optimal, which was acknowledged [17], and also linked with critical cooling rates to avoid crystallization which seem to minimize for isostatic liquids [59]. The link with the dynamics of glass-forming melts has also been established [48].

The detection of the isostatic condition in Ge-Sb-Te appears therefore crucial for the search and establishment of its GFR. Up to recently, experimental attempts to produce bulk glasses in this ternary have been limited to Sb-poor compositions close to the eutectic  $\text{Ge}_{15}\text{Te}_{85}$ , where a freezing-point depression permits us to increase viscosity to lower temperatures and to avoid crystallization [8–10], i.e., a glass transition temperature of  $T_g = 403.7$  K was found for  $\text{Ge}_{15}\text{Sb}_2\text{Te}_{83}$  [9]. As a result, the GFR of Ge-Sb-Te is partly unknown (Fig. 1, bottom) as material investigation has been essentially concentrated on phase change applications that use poor glass formers such as  $\text{Ge}_2\text{Sb}_2\text{Te}_5$  (GST225),  $\text{Ge}_1\text{Sb}_2\text{Te}_4$  (GST124), or  $\text{Ag}_4\text{In}_3\text{Sb}_{67}\text{Te}_{26}$  (AIST). Furthermore, the GFR appears to be substantially reduced when compared with the isochemical ternary Ge-Sb-Se [6] (Fig. 1, top), the binary Sb-Se leading, as for Sb-Te, to phase separation already at very low composition [60]. In this paper, we use structure models obtained from first-principles MD to determine exactly the location of a flexible-rigid transition in the canonical Ge-Sb-Te phase change material. We target compositions for which an equivalent addition of (Ge, Sb) atoms is added into the base Te

network, i.e.,  $\text{Ge}_x\text{Sb}_x\text{Te}_{100-2x}$  for different content  $x$ . Such models are first extensively compared with available experimental data. The application of MD-based constraint counting algorithms then permits us to determine a series of important results and/or findings:

(1) A flexible-to-rigid transition is found at  $x \simeq 8.5\%$ . One expects bulk glass formation to be optimized close to this composition.

(2) The angular topological constraint count leads to the identification of T-Ge sites whose population  $\eta$  decreases from  $\simeq 80\%$  in  $\text{Ge}_6\text{Sb}_6\text{Te}_{88}$  with growing  $x$ ; and for GST225, we find  $\eta = 55\%$ .

(3) Conversely, the population of Sb sites appears to change from a dominant PYR geometry encountered in Group V selenides or sulfides to a defect octahedral (O) one that is typical of  $\text{Ge}_2\text{Sb}_2\text{Te}_5$ .

A previous qualitative MD investigation on this system has been performed for select compositions and with a density functional theory (DFT) scheme that did not consider dispersion forces [61]. Since then, it has been shown that the incorporation of such corrections is crucial for the production of accurate structure models in liquid and amorphous tellurides, and the algorithms permitting us to enumerate topological constraints have been improved [62–64].

## II. NUMERICAL METHODS

### A. Generation of structure models

To detect a possible flexible-to-rigid transition and to analyze in more detail different properties emerging from the topological analysis, we have generated a certain number of different amorphous structural models of five compositions in the  $\text{Ge}_x\text{Sb}_x\text{Te}_{100-2x}$  ternary (300 K):  $x = 0\%$  (pure Te), 6%, 10%, 14%, and 22% (GST225). The calculated properties result from four independent quenches from equilibrated configurations analyzed previously in the liquid state [58,63].

All were obtained by quenching ( $\simeq 10$  K/ps) independent configurations of the equilibrated liquids obtained at 820 K (Fig. 3) and accumulating trajectories over 30–50 ps each at this temperature [63]. For all four configurations per composition, the subsequent quenching was as follows: A 600 K plateau for 20 ps followed by a relaxation at 300 K for 50 ps. The involved quenching rate is still several orders of magnitude faster than the experimental one, which is a typical feature of classical or first-principles MD simulations. However, the total energy is converging rapidly toward an asymptotic value at each temperature plateau. Furthermore, by averaging over four independent trajectories which describe possible quenched structures of the potential energy landscape, one increases the statistical accuracy of the structural model, although the detail of each configuration indicates, as it should be, that the thermal history influences essentially defects (e.g., homopolar bonding) in the structure (Fig. 4), consistently with previous studies [65]. It should be furthermore noted that such defects might also evolve with increasing relaxation time.

MD simulations of Car-Parrinello type were performed on 300-atom systems in a cubic box with periodic boundary conditions and a density equal to experimental ones [63,66].

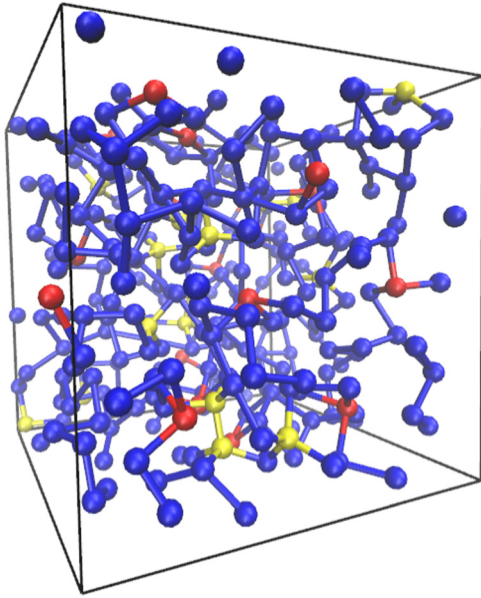


FIG. 3. Snapshot of an amorphous  $\text{Ge}_{10}\text{Sb}_{10}\text{Te}_{80}$  atomic system. Blue, red, and yellow atoms correspond to Te, Sb, and Ge atoms, respectively.

The electronic structure has been described within DFT with the inclusion of dispersion forces (DFT-D2), and evolved self-consistently during the motion (time step  $\Delta t = 0.36$  fs) using a generalized gradient approximation. Valence electrons were treated explicitly in conjunction with Troullier–Martins norm-conserving pseudopotentials using a plane-wave basis set with an energy cutoff of 20 Ry. The exchange-correlation functional was taken from Perdew–Burke–Ernzerhof (PBEsol) [66] together with DFT-D2 [67] to improve local structure (bond length) with respect to experimental findings [63].

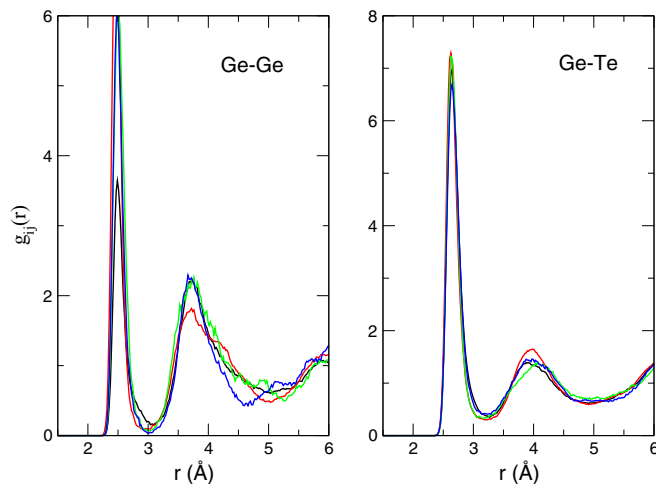


FIG. 4. Ge-Ge and Ge-Te pair correlation functions of the four independently quenched configurations of  $\text{Ge}_2\text{Sb}_2\text{Te}_5$ .

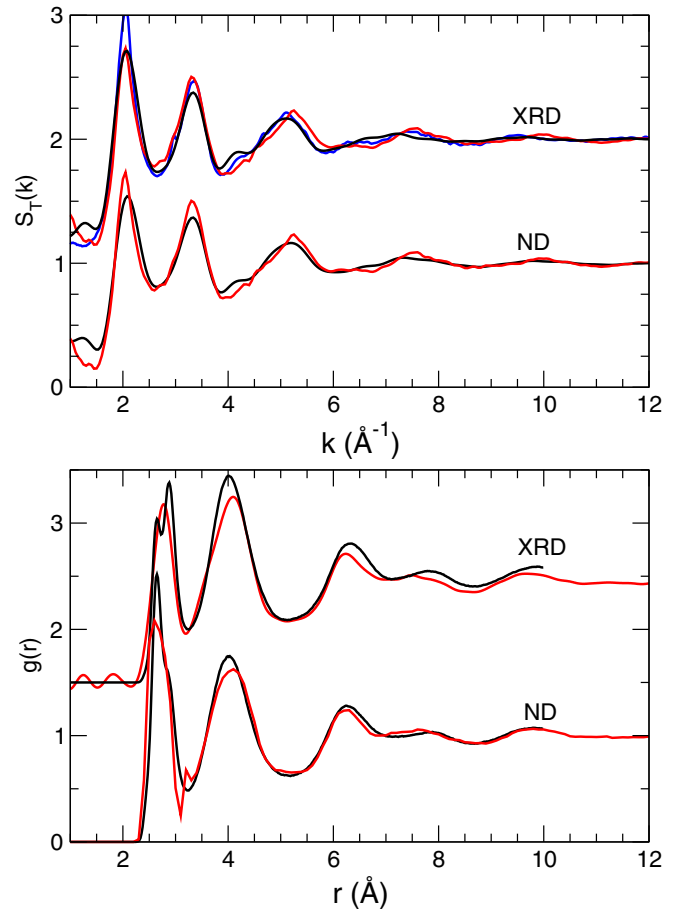


FIG. 5. (a) Calculated x-ray diffraction (XRD) and neutron diffraction (ND) structure factor  $S(k)$  (black) for amorphous  $\text{Ge}_2\text{Sb}_2\text{Te}_5$  compared with results from Kohara *et al.* (XRD, blue [68]) and Jóvári *et al.* (XRD and ND, red [69]). (b) Calculated pair correlation function  $g(r)$  for the same systems (black) and compared with experiments from Kohara *et al.* (XRD, red curve [68]) and Jóvári *et al.* (ND, red curve [69]).

## B. Model validation

The obtained structures (Fig. 3) reproduce the main features (peak positions and amplitudes) of the typical structure functions which are weighted accordingly to obtain experimental neutron diffraction (ND) or x-ray diffraction (XRD) scattering results in both reciprocal and real space (Fig. 5). Some discrepancies do appear, however, in both reciprocal and real space. Here, for the the x-ray form factors, we have used  $f_i(k) = Z_i = 32, 51,$  and  $52$  for  $i = \text{Ge}, \text{Sb},$  and  $\text{Te}$ , respectively. It should, furthermore, be noted that DFT-D2 substantially improves the structural properties with the principal peaks of the total x-ray structure factor  $S(k)$  found at  $2.0, 3.5,$  and  $5.0 \text{ \AA}^{-1}$ . Similarly, the corresponding pair correlation function  $g(r)$  is also reproduced and is dominated by Ge-Te and Sb-Te correlations, although it should be noted that an overestimation of Sb-related bond distances (Sb-Sb and Sb-Te, see below) splits the main peak of the XRD weighted  $g(r)$ . These features are reduced once compared with a neutron weighted pair correlation function [Fig. 5(b)]. Besides the first peak, we note that all secondary peaks ( $4.10$  and  $6.30 \text{ \AA}$ )



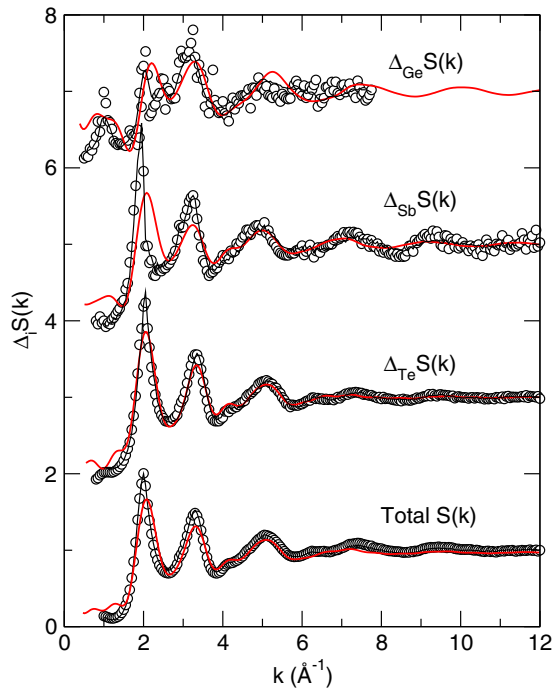


FIG. 6. Calculated difference functions  $\Delta_i S(k)$  in amorphous GST225 ( $k = \text{Ge, Sb, Te}$ , red curves) together with the total structure factor  $S(k)$  compared with experimental data accessed from anomalous x-ray scattering (AXS, circles [70]) and corresponding RMC fit (black solid lines).

are very well reproduced in terms of position and amplitude, and this provides rather good confidence that the quenched DFT structure models can be used for additional insight and analysis.

The correlations in reciprocal space can be further decoded and the structure model analyzed by comparing calculated difference functions  $\Delta_i S(k)$  from anomalous x-ray scattering (AXS) [70] (Fig. 6). Such a comparison not only provides increased information on partial structure correlations that is usually reported for lighter chalcogenides [15,16], but also constrains the models in an increased fashion. Note that the AXS weighting factors are given in Ref. [70]. The main features are reproduced from our simulations and agree with the AXS data, although one can acknowledge a slight shift of the principal peak in  $\Delta_{\text{Sb}} S(k)$  at  $k \simeq 2 \text{ \AA}^{-1}$ . The comparison indicates that structural properties at low momentum transfer are dominated by Ge correlations because of a small prepeak at  $k \simeq 1 \text{ \AA}^{-1}$  that is reproduced from our simulations, whereas  $\Delta_{\text{Ge}} S(k)$  obviously has only a small contribution [76] to the principal peaks found for the total  $S(k)$ . Conversely, both  $\Delta_{\text{Sb}} S(k)$  and  $\Delta_{\text{Te}} S(k)$ , which are perfectly reproduced from our simulations, exhibit a profile like  $S(k)$ . This furthermore signals that atomic arrangements involving Ge must be rather different from those involving Sb and Te.

The detail of bond distances  $d_{ij}$  (Table I) shows that the typical bond distances obtained from our GST225 model are compatible with previous findings, as we found 2.64 and 2.88 Å for the main Ge-Te and Sb-Te contributions that can be compared with 2.61–2.63 and 2.83–2.85 Å from extended

TABLE I. Calculated first correlating distances  $d_{ij}$  (Å) of GST225 compared with previous DFT-based simulations and experiments. The resolution for bond distances is 0.05 Å.

$i-j$	Ge-Ge	Ge-Sb	Ge-Te	Sb-Sb	Sb-Te	Te-Te
This paper	2.51	2.72	2.64	2.96	2.88	2.87
Liquid state [63]	2.53	2.72	2.69	3.00	2.92	2.92
EXAFS [71]			2.61		2.85	
EXAFS [72]	2.47		2.63		2.83	
RMC [70]	2.50		2.65		2.82	
RMC [73]	2.48	2.69	2.60		2.82	
DFT [74]		2.78		2.93		
DFT/RMC [75]	2.45	2.70	2.75	2.90	2.85	2.85

x-ray absorption fine structure (EXAFS [71,72]) experiments, respectively. While a full comparison with correlating distances is not possible due to a lack of experimental data on partial pair correlation functions (restricted to EXAFS data), our results can be put into perspective with Reverse Monte Carlo (RMC) [70,73,75], and these indicate also rather good consistency (Table I).

In Table II, we reproduce the calculated coordination numbers of the different amorphous systems, and for  $\text{Ge}_{22}\text{Sb}_{22}\text{Te}_{56}$  (GST225), we furthermore compare those results with other estimates that also strongly depend on the chosen cutoff distance [62]. We find that, for all compositions, coordination numbers differ from the 8- $\mathcal{N}$  rule, i.e.,  $n_{\text{Ge}} \simeq 3.9\text{--}4.2$ ,  $n_{\text{Sb}} \simeq 3.25$ , and  $n_{\text{Te}} \simeq 2.45\text{--}2.50$ . These numbers indicate the presence of higher coordinated species reminiscent of the O nature of crystalline GST (essentially fourfold Sb and threefold Te) and are compatible with previous investigations of GST225 or GeTe [78–80] and also to experimental results on partial correlations using AXS and associated RMC fits ( $n_{\text{Ge}} = 4.24$ ,  $n_{\text{Sb}} = 2.95$ ,  $n_{\text{Te}} = 2.30$  [70,76]). Note that the inclusion of dispersion forces (i.e., DFT-D2) leads to an overall reduction of both the coordination numbers and the bond lengths with respect to regular DFT, as already acknowledged in Ge-Sb-Te liquids [63].

TABLE II. Calculated coordination numbers  $n_i$  at different compositions  $x$  in amorphous  $\text{Ge}_x\text{Sb}_x\text{Te}_{1-2x}$  at the cutoff distance  $r_m = 3.2 \text{ \AA}$  determined from the minimum of corresponding functions  $g_i(r)$ . Corresponding evaluations are also given for GST225 [74–76].

System	$n_{\text{Ge}}$	$n_{\text{Sb}}$	$n_{\text{Te}}$
Te	—	—	$2.53 \pm 0.05$
DFT [77]	—	—	2.39
$\text{Ge}_6\text{Sb}_6\text{Te}_{88}$	$4.05 \pm 0.05$	$3.23 \pm 0.05$	$2.46 \pm 0.05$
$\text{Ge}_{10}\text{Sb}_{10}\text{Te}_{80}$	$3.93 \pm 0.05$	$3.24 \pm 0.05$	$2.46 \pm 0.05$
$\text{Ge}_{14}\text{Sb}_{14}\text{Te}_{72}$	$4.14 \pm 0.05$	$3.25 \pm 0.05$	$2.50 \pm 0.05$
$\text{Ge}_{22}\text{Sb}_{22}\text{Te}_{56}$	$4.07 \pm 0.05$	$3.27 \pm 0.05$	$2.45 \pm 0.05$
RMC [76]	4.24	2.95	2.30
DFT [74]	4.20	3.70	2.90
DFT/RMC [75]	3.92	3.41	2.56

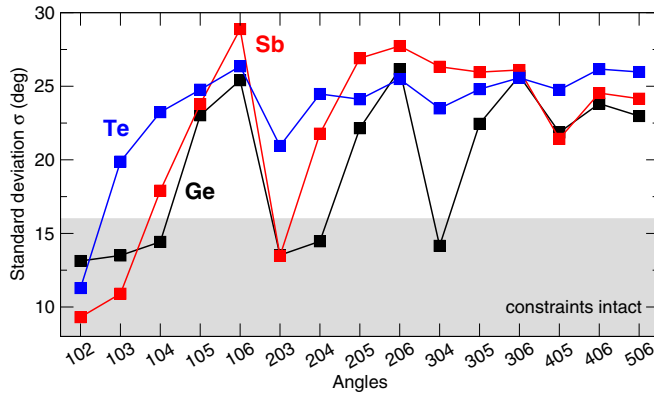


FIG. 7. Calculated angular second moment  $\sigma$  of Ge, Sb, and Te atoms in amorphous  $\text{Ge}_{14}\text{Sb}_{14}\text{Te}_{72}$  for all possible angles  $i0j$  ( $i, j = 1, 6$ ). For individual constraint calculations,  $\sigma_m = 16^\circ$  is used (see text for details).

We are not aware of other experimental structure data for the other investigated compositions on the  $\text{Ge}_x\text{Sb}_x\text{Te}_{100-2x}$  join.

### C. Topological analysis

To obtain the atomic density of BS constraints  $n_c^{\text{BS}}(i)$ , we use species-centered correlation function  $[g_i(r)]$ , a combination of pair functions  $g_{ij}(r)$  and  $i = \text{Ge, Sb, Te}$ , and the integration up to the first minimum  $r_m = 3.20 \text{ \AA}$  of  $g_i(r)$  gives the coordination numbers  $r_i = 2n_c^{\text{BS}}(i)$  [21].

#### 1. Average constraints

The average BB constraint counting  $n_c^{\text{BB}}$  from MD simulations is based on partial bond angle distributions (PBADs) and defined by (i) selecting for each type  $k$  ( $k = \text{Ge, Sb, Te}$ ) of a central atom 0 the  $N$  first neighbors leading to  $N(N-1)/2$  possible angles ( $N = 6$  hereafter) and (ii) calculating all possible PBADs to extract their corresponding second moment (standard deviation  $\sigma$ ), which provides a quantitative estimate of the angular excursion around the mean angle, thus verifying if the corresponding angle acts as a rigid constraint. Small  $\sigma$  values correspond, indeed, to an intact BB constraint which maintains a rigid angle at a fixed value, whereas a large  $\sigma$  corresponds to a BB weakness, giving rise to an ineffective constraint.

Figure 7 shows the application of such an average treatment on the obtained amorphous  $\text{Ge}_{14}\text{Sb}_{14}\text{Te}_{72}$  model, where the species-related standard deviation  $\sigma$  for the 15 different PBADs is represented as a function of the corresponding angle (from 102 up to 506). The trend clearly acknowledges two different populations separated by a gap in  $\sigma$ , i.e., those for which  $\sigma$  is small ( $8^\circ \leq \sigma \leq 15^\circ$ ) and which are associated with intact angular constraints and those displaying  $\sigma \geq 20^\circ$  that are ineffective from the viewpoint of rigidity. It should be noted that the germanium-related data exhibit six small values for  $\sigma$  but result from two possible populations: a T-Ge with six small  $\sigma$  values and a PYR or defect O-Ge with only three small  $\sigma$  values. The average treatment does not permit us to distinguish both populations, and therefore, an individual MD-based BB count is necessary [24], as presented next.

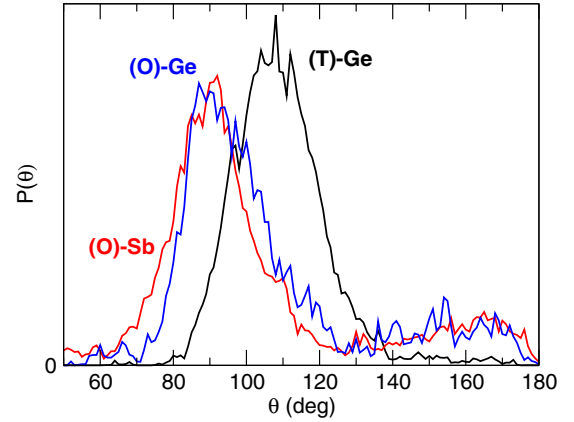


FIG. 8. (a) Bond angle distribution of identified tetrahedral (T)-Ge, octahedral (O)-Ge, and O-Sb geometries in amorphous  $\text{Ge}_{22}\text{Sb}_{22}\text{Te}_{56}$  (GST225). Note that the identification of the geometries relies only on the number of intact bond-bending (BB) constraints (i.e.,  $\sigma_k$ ), not on the angles themselves (i.e.,  $\bar{\theta}_k$ ).

#### 2. Individual constraints

To obtain a detailed analysis, angular constraints can also be tracked individually during the course of the MD simulation. In this case, for each individual atom  $k$ , a single bond angle distribution (BAD) is calculated together with its average value  $\bar{\theta}_k$  over the trajectory (the first moment of the distribution  $k$ ) and a second moment  $\sigma_k$ . A cutoff of  $\sigma_k = \sigma_m = 16^\circ$  is chosen to determine if a constraint is intact or broken, based on what has been previously obtained on average. This value corresponds to the lower bound of  $\sigma$  for averaged intact constraints (Fig. 7). Once these angles are tracked individually during the simulation, one can identify a Ge tetrahedron [(T)-Ge] if six rigid angles are found which give rise to six corresponding low standard deviations [14]. The remaining angles which do not fulfill this criterion usually have only three low standard deviations and are, therefore, identified as PYR geometries or defect octahedra [(O)-Ge] as for the Sb species [(O)-Sb] in the present systems. Averages over the entire system then lead to a precise fraction  $\eta$  of (T)-Ge with thermodynamic conditions or composition. Such fractions can eventually be compared with Mössbauer spectroscopy of  $^{119}\text{Sn}$  substituted tellurides which probes the local geometry, T vs O [4,14,81,82] because nuclear hyperfine signals are directly transferable to those measured in T or O reference compounds [83].

Figure 8 exemplifies the method of individual constraints which can lead to geometry-dependent BADs. Based on the selection criteria of  $\sigma_k$  alone, it is interesting to note that the obtained BADs satisfying six and three rigid angular constraints are centered at  $\bar{\theta}_{\text{Ge}} = 109^\circ$  and  $90^\circ$ , respectively. The latter BAD furthermore contains a broad contribution close to  $180^\circ$  that permits us to unambiguously identify defect O sites for some Sb and Ge atoms.

### III. RESULTS AND DISCUSSION

We now turn to the main results of this contribution, that is, the determination of the locus of the rigidity transition.

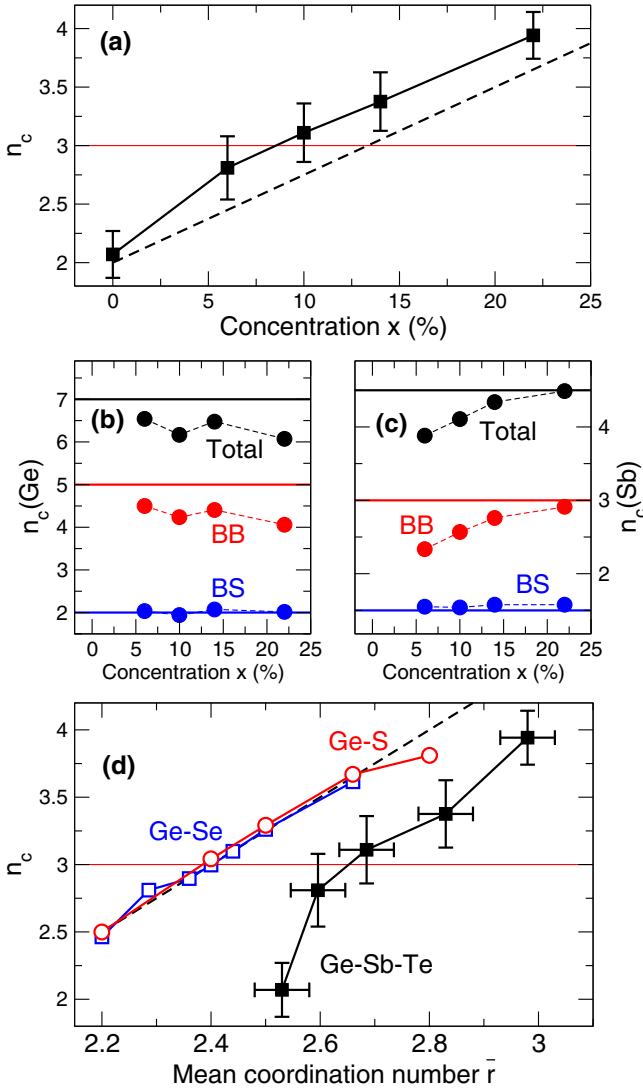


FIG. 9. (a) Calculated fraction of topological constraints  $n_c$  in amorphous  $\text{Ge}_x\text{Sb}_x\text{Te}_{100-2x}$  as a function of the composition  $x$ . The broken line corresponds to the mean-field estimate  $n_c = 2 + 7x/2$  [39]. (b) Ge-related and (c) Sb-related topological constraints [total, bond-stretching (BS), and bond-bending (BB)] as a function of  $x$  (symbols). The horizontal lines correspond to the expected values if the 8- $\mathcal{N}$  rule applies. (d) Calculated fraction of topological constraints  $n_c$  [same as (a)] as a function of the network mean coordination number  $\bar{r}$ . Comparison with Ge-S [34] and Ge-Se glasses [54]. The broken line corresponds with the mean-field estimate  $n_c = \frac{5}{2}\bar{r} - 3$ .

### A. Flexible-to-rigid transition

Using the methods described above, we have calculated the BS and BB constraint density in the different amorphous systems.

Figure 9(a) represents the constraint density as a function of the content  $x$ . It is seen that, as expected,  $n_c$  grows with increasing atomic cross-link density as it does in all modified chalcogenides. An isostatic condition corresponding to a flexible-to-rigid transition is expected for compositions close to the compound  $\text{Ge}_{8.5}\text{Sb}_{8.5}\text{Te}_{83}$ , i.e.,  $x_c = 8.5\%$ . This location is found to be somewhat lower than the one usually

determined from a mean-field constraint count with a full application of the 8- $\mathcal{N}$  rule as in the isochemical Ge-As-Se compound [39]. In this case, one has  $n_c = 2(1 - 2x) + 7x + \frac{9}{2}x$  and  $x_c = 13.3\%$  [broken line in Fig. 9(a)]. The present analysis, thus, suggests that, when compared with selenide or sulfide analogs, the Ge-Sb-Te stiffens earlier during the course of structural modification induced by the addition of (Ge, Sb) atoms (see below). The detail of the different topological contributions reveals that, while the BS density remains more or less constant which is indicative of a constant coordination number  $r$  for Ge and Sb atoms [Table II and Figs. 9(b) and 9(c)], BB constraints evolve with  $x$ . This situation is at variance with selenides and sulfides, where  $n_c^{\text{BB}} = 2r - 3$  is independent of composition and  $n_c^{\text{BB}} = 7$  and 3 for Ge and Sb, respectively. The evolution of  $n_c^{\text{BB}}$  with  $x$  results from the presence of mixed geometries (T, defect octrahedral) that are specific to these tellurides. Here, one notices that one always has  $n_c^{\text{BB}}(\text{Ge}) < 5$  [Fig. 9(b)], which is indicative of a network having  $< 100\%$  tetrahedra [15]. Conversely, the Sb atom displays an opposite trend with  $x$ , and for the GST225 composition, it nearly approaches the value of  $n_c^{\text{BB}} = 3$  expected for Group V chalcogenides when the 8- $\mathcal{N}$  rule applies. We discuss the detail of the Sb geometries in the following.

While Ge- and Sb-related constraints appear to be less rigid than in corresponding selenides and sulfides, the increased rigidity observed for the entire system arises essentially from the Te atoms [Fig. 10(a)].

In fact, except for elemental Te for which the density of BB constraints is slightly less than  $n_c^{\text{BB}} = 1$  because of the presence of dangling bonds (onefold or terminal chain Te), one acknowledges a systematic increase of angular stiffening, the number of BS constraint remaining constant and close to a value of  $n_c^{\text{BS}} \simeq 1.16(5)$ . Instead of remaining constant at a fixed value of  $n_c = 2$  as in sulfides,  $n_c(\text{Te})$  now increases steadily from 2.07(0) for elemental Te up to 2.47(8) for GST225.

As a result, the *locus* of the mean-field flexible-rigid transition, which is usually found at the average coordination number of  $\bar{r} = 2.4$ , is shifted to higher  $\bar{r}$  in the present tellurides. Using the coordination numbers determined from the simulation (Table II), we find, indeed, that the composition  $x = 8.5\%$  corresponds with a network mean coordination number  $\bar{r} = 2.65(8)$  which is also larger than the location of the dynamic anomaly obtained [9] for the isochemical Ge-As-Te system ( $\bar{r} \simeq 2.5$ , Fig. 2). Overall,  $n_c$  scales as

$$n_c(x) = \left(1 + \frac{r_{\text{Te}}}{2}\right) + \frac{1}{2} \left(r_{\text{Sb}} - 2r_{\text{Te}}\right)x + \left[6 + 2\eta(x)\right]x, \quad (2)$$

where it has been assumed that (i)  $r_{\text{Ge}} = 4$  (Table II) and Ge exist in two local geometries with a fraction  $\eta(x)$  of tetrahedra, (ii)  $r_{\text{Sb}} > 3$ , but always has  $n_c^{\text{BB}} = 3$ , and (iii)  $r_{\text{Te}} > 2$ .

### B. Comparison with other simulated chalcogenides

It is interesting to compare the present findings with previous results obtained from the application of MD-based constraint counting algorithms to other chalcogenides.

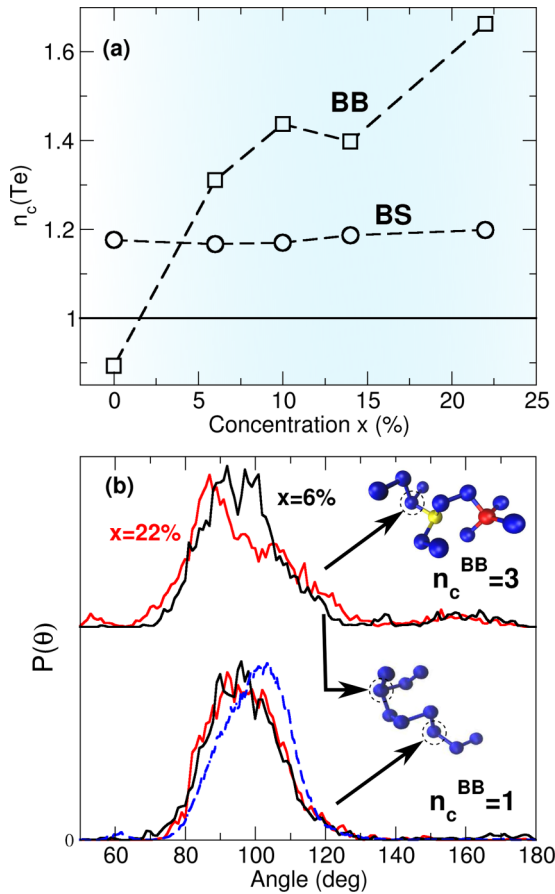


FIG. 10. (a) Calculated fraction of tellurium-related topological bond-stretching (BS) (circles) and bond-bending (BB) constraints (boxes) in amorphous  $\text{Ge}_x\text{Sb}_x\text{Te}_{100-2x}$  as a function of the composition  $x$ . The black horizontal line  $n_c = 1$  is the expected value from the  $8-\mathcal{N}$  rule for BS and BB constraints. (b) Te-centered bond angle distributions (BADs) of  $\text{Ge}_6\text{Sb}_6\text{Te}_{88}$  (black) and  $\text{Ge}_{22}\text{Sb}_{22}\text{Te}_{56}$  (GST225, red) according to the presence of 1 or 3 BB constraints. The broken blue curve corresponds to Se-centered BAD in amorphous  $\text{As}_2\text{Se}_3$  [89]. Fragments of the atomic structure containing threefold Te (blue atoms) with  $n_c^{\text{BB}} = 3$  and twofold Te ( $n_c^{\text{BB}} = 1$ ) are indicated. Sb and Ge atoms are in yellow and red, respectively.

Figure 9(d) represents the constraint density  $n_c$  now represented as a function of the mean coordination number  $\bar{r}$  for Ge-Sb-Te, contrasted to Ge-S [34] and Ge-Se [54] glasses. For both Ge-based binary glasses, the shift to low  $\bar{r}$  is related to coordination numbers fulfilling exactly the  $8-\mathcal{N}$  rule, and in this case, the numerical estimate of  $n_c$  matches the mean-field density of constraints [21] given by  $n_c = \frac{5}{2}\bar{r} - 3$  that merely satisfies the isostatic criterion for  $\bar{r} \simeq 2.4$  [broken line, Fig. 9(d)]. As mentioned before, the peculiar constraint behavior of Ge-Sb-Te results from two major differences with respect to the Ge-S and Ge-Se compounds. First, the breakdown of the  $8-\mathcal{N}$  rule (Table II) leads to a systematic increase for all compositions of  $n_i$  ( $i = \text{Sb}, \text{Te}$ ) with respect to the reference values  $n_{\text{Sb}} = 3$  and  $n_{\text{Te}} = 2$  and produces a subsequent increase of  $\bar{r}$ . The resulting shift appears, thus, to be specific to the telluride compounds because the isochemical Ge-Sb-Se is found to also follow the usual mean-field  $n_c = \frac{5}{2}\bar{r} - 3$  behavior [6]. Second, we have stressed above

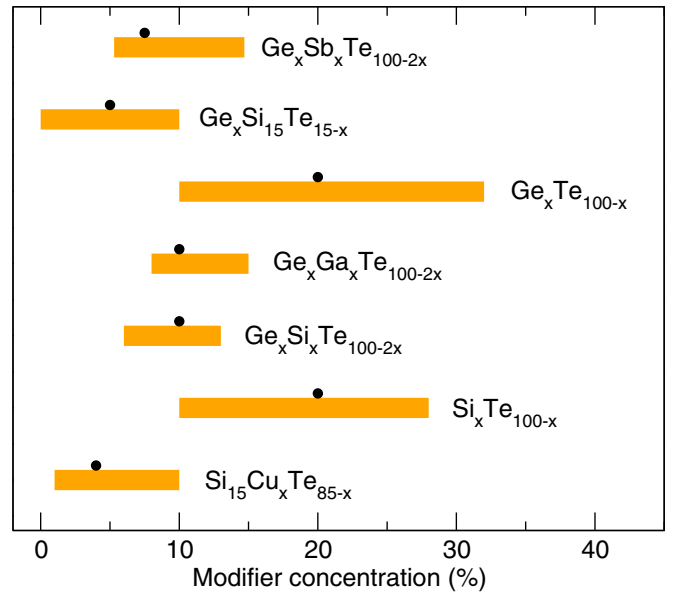


FIG. 11. Glass-forming region (GFR; bars) and locus of the flexible-rigid transition satisfying the Maxwell stability criterion  $n_c = 3$  (filled circles) in  $\text{Ge}_x\text{Sb}_x\text{Te}_{100-2x}$  (this paper) compared with the GFR determined experimentally from co-evaporation techniques [84]. Various telluride glasses are also reported from the literature:  $\text{Ge}_x\text{Si}_{15}\text{Te}_{85-x}$  [40,85],  $\text{Ge}_x\text{Ga}_x\text{Te}_{100-2x}$  [3],  $\text{Ge}_x\text{Si}_x\text{Te}_{100-2x}$  [4],  $\text{Si}_x\text{Te}_{100-x}$  [86], and  $\text{Si}_{15}\text{Cu}_x\text{Te}_{85-x}$  [43].

that  $n_c = n_c^{\text{BB}}$  also differs when compared with Ge-S and Ge-Se as the Ge and Sb BB density is always lower than the “reference” values of  $n_c^{\text{BB}} = 5$  and 3, respectively [Fig. 9(b) and 9(c)]. The reduction of such constraints is compensated by an increased rigidity of Te [Fig. 10(a)] that contrasts with the constant value  $n_c^{\text{BB}} = 1$  for selenium and sulfur.

### C. Comparison with experiments

The locus of the flexible-to-rigid transition at  $x \simeq 8.5\%$  can now be compared with experimental results. Recently, using thermal co-evaporation techniques, glass formation in the Ge-Sb-Te system has been examined along the same compositional join [84]. Noteworthy is the fact the glass-forming range of  $\text{Ge}_x\text{Sb}_x\text{Te}_{100-2x}$  glasses extends from the locus  $x_c$  of the rigidity transition (Fig. 11) on both sides (chalcogen rich and chalcogen poor) with  $5.5\% \leq x \leq 14.7\%$ . A perusal of the GFR of different melt-quenched telluride glasses (Fig. 11) shows that the flexible-to-rigid transition is systematically found within the GFR for different telluride systems involving, e.g., Group IV and V elements. These observed features are compatible with the earlier established correlations linking the isostatic criterion with optimal glass formation [17,25].

In Ref. [84], it has been furthermore detected that the optical band gap  $E_g(x)$  in  $\text{Ge}_x\text{Sb}_x\text{Te}_{100-2x}$  displays a maximum at  $x_c$ , and this drives the anomalous conductivity behavior of the amorphous phase and also the ageing behavior [87]. For a parent system ( $\text{Ge}_x\text{Te}_{100-x}$  [88]), it was argued that the Maxwell stability condition defining a flexible-to-stress transition could be detected from conductivity measurements because stressed rigid glasses ( $x > x_c = 26.5\%$ ) were exhibiting a rather strong



resistance drift with time, the optical band gap  $E_g(x)$  leading to a maximum for  $x_c$ . These results indicate a globally consistent behavior for two binary and ternary tellurides and also suggest that anomalies (as those initially represented in Fig. 2) can also be detected from optical and/or electric properties at the flexible-to-rigid transition.

#### D. Constraints in detail

The nature of the Te-centered BADs in Ge-Sb-Te can be analyzed [Fig. 10(b)] by separating Te populations according to the presence of one ( $n_c^{\text{BB}} = 1$ ) or three BB constraints ( $n_c^{\text{BB}} = 3$ ). According to TCT, each new bond added onto a central  $r$ -fold atom needs, indeed, the definition of two additional angles as  $n_c^{\text{BB}} = (2r - 3)$  [21]. Figure 10(b) now represents for two compositions the related BADs fulfilling either  $n_c^{\text{BB}} = 1$  or 3. The former appears to be nearly independent of composition, with an average angle  $\bar{\theta} > 90^\circ$  and resembles the one obtained for a typical selenide glass [89] for which coordination change for the chalcogen atom is absent. These features are at variance with those determined for Te atoms fulfilling  $n_c^{\text{BB}} = 3$  which appear to have an angular topology obviously influenced by Ge/Sb content, and centered in GST225 at angles typical of an O environment (see below).

This dramatic increase in  $n_c^{\text{BB}}$  (Te) can be decoded further by examining each Te atom individually [Fig. 12(a)] or by classifying them according to their mechanical character [Fig. 12(b)]. It is, indeed, detected that increased miscoordinations appear for Te atoms with increasing connectivity or  $x$  as manifested by the constraint histograms [panel (a)]. For elemental Te, the picture is compatible with previous numerical investigations [66,77], i.e., the Te network is essentially made of Te chains but with a coordination number that is slightly  $>2$ , as also acknowledged from neutron scattering experiments [13]. The twofold atoms are the most abundant; additional terminals (onfold Te) are found and also overcoordinated atoms which act as cross-links for the chains and form fragments of network regions. These arise from longer bonds. Interestingly, these extra bonds do not initially give rise to additional rigid angular constraints so that, except for terminal Te, one always has  $n_c^{\text{BB}} = 1$  per atom in elemental Te [Figs. 10(a) and 12(c)] and  $n_c = 2.07(0)$ , as mentioned above. The possible defect angular topologies only lead to flexibility that slightly decrease with addition of (Ge, Sb) cross-links as less and less chain fragments become available [black curve, Fig. 12(c)].

The addition of Ge/Sb content in  $\text{Ge}_x\text{Sb}_x\text{Te}_{100-2x}$  now deeply impacts the topology of the Te subnetwork as the additional angles arising from third neighbor contributions stiffen as  $x \neq 0$  and lead to a secondary contribution centered at  $n_c = 4.5$  [Fig. 12(a)] identified with threefold coordinated Te as  $n_c = r/2 + (2r - 3)$  [24] leads to  $n_c = 4.5$  for  $r = 3$ , typical of threefold coordinated atoms. This contribution is found to increase up to GST225, and as Te atoms are selected according to their number of rigid constraints ( $n_c^{\text{BB}} = 1$  or 3), corresponding BADs display, as described above, a rather different profile [Fig. 10(b)]. For  $n_c^{\text{BB}} = 1$ , the distribution is centered at  $\simeq 97^\circ$ , like a Se-centered BAD in  $\text{As}_2\text{Se}_3$  [89], and appears to be weakly sensitive to composition as differences

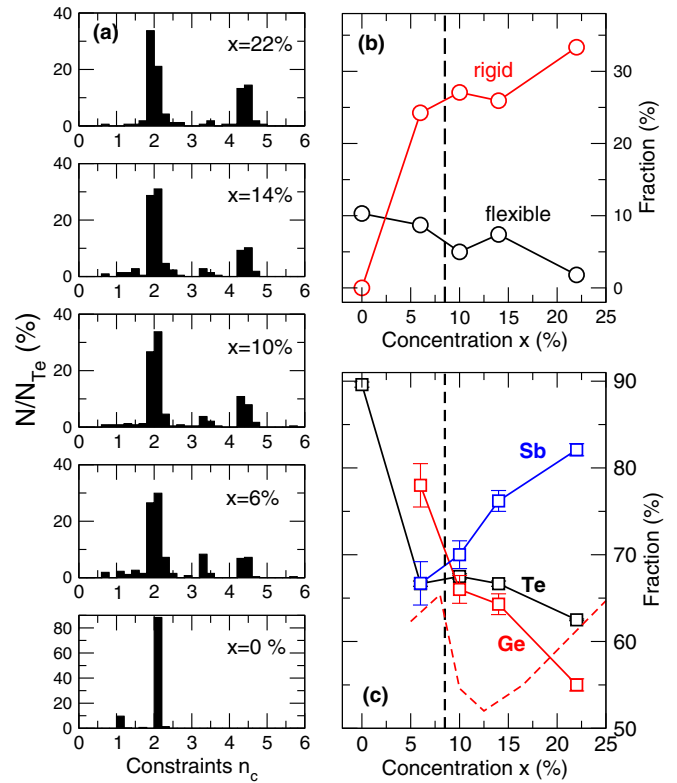


FIG. 12. (a) Five histograms showing the distribution of total Te-related topological constraints at various compositions in amorphous  $\text{Ge}_x\text{Sb}_x\text{Te}_{100-2x}$ . (b) Calculated fraction of Te defect topologies as a function of composition  $x$  exhibiting  $n_c > 2$  (rigid, red) and  $n_c < 2$  (flexible, black). (c) Population of perfect  $8-\mathcal{N}$  topologies: tetrahedral (T)-Ge with  $n_c^{\text{BB}} = 5$ , Sb with  $n_c^{\text{BB}} = 3$ , and Te with  $n_c^{\text{BB}} = 1$ . The red broken line represents the calculated fraction  $\eta$  of Ge tetrahedra in  $\text{Ge}_x\text{Te}_{100-x}$  [81] appropriately rescaled on the  $x$  axis (see text for details). The broken vertical lines in (b) and (c) indicate the *locus* of the flexible-to-rigid transition at  $x_c = 8.5\%$ .

in the  $\text{Ge}_6\text{Sb}_6\text{Te}_{88}$  and GST225 BADs are negligible. It can, thus, be concluded that such Te atoms behave as their (S, Se) chemical analogs. For a more rigid environment [ $n_c = 3$ , Fig. 10(b) top], one finds Te to be in a defect O geometry that manifests by a main peak at  $88-92^\circ$  depending on composition and a contribution at  $180^\circ$ .

An additional means to decode the growth of Te rigidity is to calculate the fraction of atoms fulfilling either  $n_c > 2$  or  $n_c < 2$ , which corresponds to atoms being more or less rigid compared with the selenide counterpart, respectively. The result shows an overall increase of rigid Te [Fig. 12(b)], whereas the population of perfect topologies satisfying the  $8-\mathcal{N}$  rule decreases continuously [Fig. 12(c)].

#### E. Evolutive geometries

The detailed investigation using individual angular constraints to determine the nature of short-range order also permits us to infer the presence of geometries that are sensitive to chemical composition.

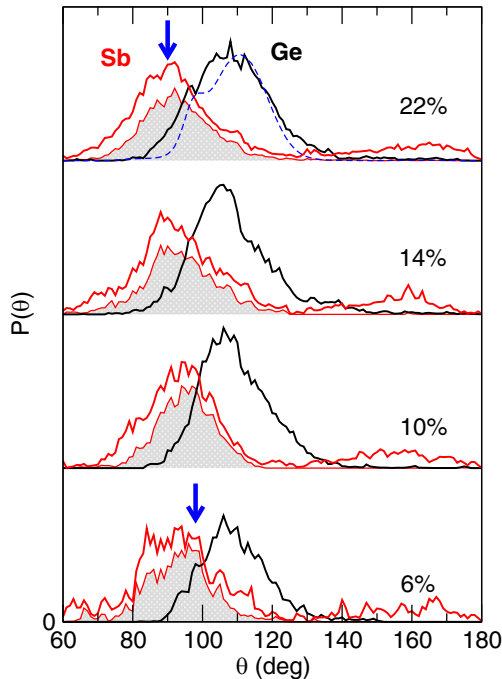


FIG. 13. Bond angle distribution (BAD) of tetrahedral (T)-Ge and Sb geometries using the identification criteria from the number of topological constraints T-Ge to satisfy  $n_c^{BB} = 5$  (black curves). The Sb BAD is represented either totally (red curve) or by selecting them from the condition  $n_c^{BB} = 3$  (gray area, see text for details). The broken blue curve corresponds to a S-Ge-S BAD calculated for  $\text{GeS}_2$  [90]. Blue arrows indicate  $98^\circ$  (pyramidal geometry) and  $90^\circ$  (octahedral geometry).

### 1. Population of tetrahedra

Figure 13 represents Ge- and Sb-centered BADs fulfilling certain selection criteria based on angular constraints, now represented for different compositions. It is seen that Ge atoms fulfilling  $n_c^{BB} = 5$  display a BAD that is centered at the T angle of  $\theta_T = \arccos(-\frac{1}{3}) = 109^\circ 47'$ . For GST225, the distribution is broad (same as Fig. 8) and like the one determined for  $\text{GeS}_2$  [90] (blue broken line). The residual distribution consists of essentially signatures from O-Ge (Fig. 8). With decreasing Ge/Sb content, the distribution displays an obvious tail at angles  $\theta > \theta_T$ . This evolution has been previously obtained for  $\text{GeTe}_2$  [81] and interpreted as a mixture of tetrahedra containing possible Ge-Ge homopolar bonds. The deviation from  $\theta_T$  to larger angles is found in strained molecules such as, e.g., fenestranes [91], a class of materials where the bond lengths deviate from those found in reference alkanes and induce a bond angle at the central carbon atom of around  $130^\circ$ . The mechanism of “planarization” of the T carbon results from a gradual increase in bond angle deformation and strain energy that affect a change in hybridization [92]. For the  $\text{Ge}_x\text{Sb}_x\text{Te}_{100-2x}$  system, this secondary T population appears to be an intermediate geometry between the regular (T) and the O geometry.

The population of tetrahedra can be calculated as a function of Ge/Sb content, and results indicate that the presence of increasing stress (or  $x$ ) induces a progressive (T) to (O) conversion [Fig. 12(c)] as  $\eta$  continuously decreases from 78.0%

in  $\text{Ge}_6\text{Sb}_6\text{Te}_{88}$  to 55.1% in  $\text{Ge}_{22}\text{Sb}_{22}\text{Te}_{56}$  (GST225), at variance with the calculated evolution of  $\eta(x)$  in the binary Ge-Te. This system exhibited, indeed, a minimal value of T population for  $\text{GeTe}_3$  [81], i.e., for a concentration of Te atoms of 75% which is equivalent in the present system to  $x = 12.5\%$  [red broken line in Fig. 12(c), data are appropriately rescaled by a factor of 2 on the  $x$  axis]. The fraction of  $\eta = 55.1\%$  found for GST225 is substantially larger than the one determined in previous studies of GST225 (33% [93]) or on  $\text{Ge}_1\text{Sb}_2\text{Te}_4$  (21% [94]) using different analysis methods (for a discussion on the accuracy of the methods, see Ref. [14]). As a reminder, the inclusion of dispersion forces leads to a global reduction of the Ge-Te bond lengths which in turn increases the population of tetrahedra as exemplified recently for the GeTe system where  $\eta = 64.7\%$  and  $41.2\%$  for DFT-D2 and DFT, respectively. The present calculation showing a majority of (T)-Ge in GST225 is supported by recent  $^{119}\text{Sn}$  Mössbauer spectroscopy [82]. In fact, isomer shifts indicate that tin atoms substitute germanium atomic sites and form  $sp^3$  tetrahedra, and corresponding spectra exhibit a single line typical of Ge-T sites.

### 2. T stiffness

To access the rigidity of the Ge tetrahedra, we build on an analysis developed recently [81] that interprets the BADs in terms of an effective potential  $U_{\text{eff}}(\theta)$ , assuming that one has

$$P(\cos \theta) \propto \exp[U_{\text{eff}}(\theta)/k_B T], \quad (3)$$

as introduced in studies on liquid-liquid transitions of silica [95]. It is, furthermore, assumed that the effective potential is harmonic with a stiffness constant  $k_2(x)$ , i.e.,  $U_{\text{eff}}(\theta) = \frac{1}{2}k_2(x)(\theta - \theta_T)^2$ , and  $\theta_T$  being the T angle. Using Eq. (3), the different Ge-related BADs of Fig. 13 can be fitted (Fig. 14) to extract a stiffness  $k_2$  that is represented as a function of Ge content (inset). One should also note that (i)  $\theta_T$  is left as an adjustable parameter, and the fits lead to values that are always found in the range of the T angle ( $105^\circ$ – $107^\circ$ ), (ii) a second distribution [shaded gray, Fig. 14(a)] of the form of Eq. (3) is needed because of the presence of the tail at  $\theta > \theta_T$ , which is especially visible for  $\text{Ge}_{10}\text{Sb}_{10}\text{Te}_{80}$  and  $\text{Ge}_{14}\text{Sb}_{14}\text{Te}_{72}$  (Fig. 13). This second contribution involves a fitted mean angle of  $\theta_T = 117.0^\circ$  and  $116.7(8)^\circ$  for  $x = 6\%$  and  $22\%$ , respectively. Corresponding stiffness constants are represented in the inset of Fig. 14(a), and these (red circles) are found to be systematically smaller than the dominant contribution (black circles). The detailed analysis of the Ge-centered BADs shows that the former contribution is associated with a Ge-Ge-Te BAD (not shown), the emergence of such motifs being linked with the growing presence of homopolar bonds in the structure which already give rise to a typical angle.

Corresponding Ge-centered pair correlation functions  $g_i(r)$  are calculated from the neighbor distributions [61], and these indicate that tetrahedra lead to a more structured shell of first and second neighbors [Fig. 14(b)], the minimum obtained at  $r = r_m \simeq 3.2 \text{ \AA}$ , leading to a lower value for  $g_{\text{Ge}}(r_m)$  when compared with the same calculation for the total number of Ge atoms of the system (black line). These features

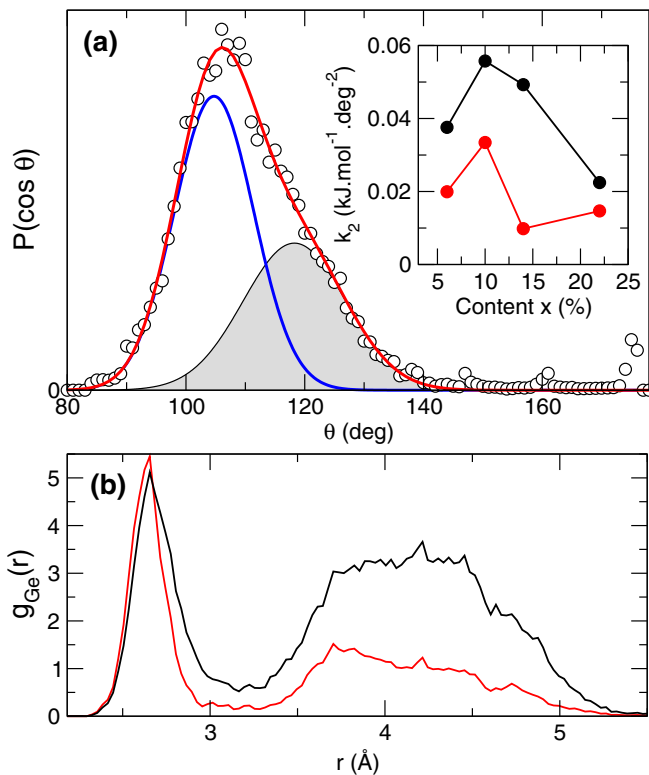


FIG. 14. (a) Fit of  $P(\cos\theta)$  using Eq. (3) for the  $\text{Ge}_{10}\text{Sb}_{10}\text{Te}_{80}$  compound, using a majority (blue curve) and a minority (T)-mode (shaded gray). The inset shows the evolution of the stiffness  $k_2$  with composition for the main mode (black,  $\theta \simeq \theta_T$ ) and the mode with  $\theta > \theta_T$  (red curve). (b) Calculated pair correlation function  $g_{\text{Ge}}(r)$  in GST225: Total (black curve) and function calculated only for identified Ge tetrahedra (red).

are typical of T chalcogenides, and in  $\text{GeSe}_2$ , one usually has  $g_{\text{Ge}}(r_m) \simeq 0$  [15].

### 3. From PYR to defect O antimony

A similar analysis is performed for the Sb atoms, and Fig. 13 highlights the main features obtained. The Sb-centered BAD consists of a broad distribution at  $80^\circ$ – $110^\circ$  and a secondary peak at  $180^\circ$ , as already acknowledged in the liquid [63] and in the amorphous state [78], where it was found that the Sb geometry is O in GST225.

We select, again, atoms according to a BB criteria expected from the  $8-\mathcal{N}$  rule prevailing in lighter Sb chalcogenides. In such materials, the pnictide (Group V, i.e., P, As, and Sb) atoms usually form trigonal PYRs such as  $\text{AsSe}_{3/2}$  with typical angles of  $98^\circ$  [1], and these involve three angular topological constraints so that  $n_c^{\text{BB}} = 3$ . We select Sb atoms fulfilling this criterion together with  $r_{\text{Sb}} = 3$ , and corresponding BADs are represented in Fig. 13 (gray distributions). It is seen that, at low Sb/Ge content, such Sb atoms essentially behave as in other typical selenides or sulfides, i.e., they have three neighbors, and the three rigid Sb-centered angles (mostly Te-Sb-Te) are found at an angle of  $98^\circ$  typical of the PYR geometry (arrow in Fig. 13 for the composition of 6%), without any contribution at  $\theta \simeq 180^\circ$ . The population of such PYR units appears to be dominant, as about 65% are found in

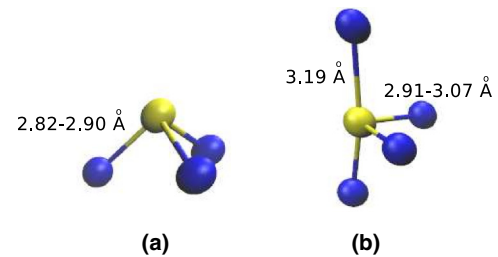


FIG. 15. Local Sb geometries detected in amorphous Ge-Sb-Te. (a) Pyramidal (PYR) unit and (b) defect octahedral unit. Typical involved bond distances are indicated.

$\text{Ge}_6\text{Sb}_6\text{Te}_{88}$  [Fig. 12(c)]. An inspection of the structures obtained (Fig. 15) permits us, indeed, to identify both geometries in  $\text{Ge}_6\text{Sb}_6\text{Te}_{88}$  and  $\text{Ge}_{10}\text{Sb}_{10}\text{Te}_{80}$ , and it is furthermore noted that the PYR involves bond distances that are slightly smaller ( $2.82$ – $2.90$  Å) when compared with the distances defining the equatorial plane in (O)-Sb ( $2.91$ – $3.07$  Å). Note that longer bonds perpendicular to the equatorial plane do exist ( $3.19$  Å). The typical average PYR angle maintains up to  $x = 10$ – $14\%$ , but then shifts to about  $90^\circ$  (second blue arrow in Fig. 13), which signals that, for GST225, the dominant geometry is, indeed, defect O with threefold or fourfold coordinated Sb (Table II).

## IV. SUMMARY AND CONCLUSIONS

Here, we have investigated the possibility of a flexible-to-rigid transition in Ge-Sb-Te, which is a system of important interest due to its potential applications in optoelectronics and data storage, and given that one should expect rigidity to onset with increasing cross-link density, as in many other glassy chalcogenides.

Using DFT-based MD simulations, we have generated different structure models along the join of  $\text{Ge}_x\text{Sb}_x\text{Te}_{100-2x}$  and investigated the topology of the underlying networks. By enumerating BS and BB constraints from dedicated algorithms, we have been able to establish the *locus* of a flexible-to-rigid transition at  $x \simeq 8.5\%$ , i.e., for the  $\text{Ge}_{8.5}\text{Sb}_{8.5}\text{Te}_{83}$  compound corresponding to a higher average network coordination number [ $\bar{r} = 2.65(8)$ ] than the one usually obtained when all BS and BB constraints are intact and no dangling bonds are present. Having in mind that glass-forming ability is increased in isostatic networks [20], bulk glass formation should be possible close to this composition and might extend the glass-forming domain, which is experimentally restricted at this stage to Sb-poor compositions close to the binary Ge-Te glasses. Work in this direction is in progress [84].

The second main outcome of this contribution is the use of the angular constraint counting algorithms to identify T-Ge, O, and PYR Sb sites in the structure. With growing Ge/Sb content, (T)-Ge and (PYR)-Sb both decrease, although for GST225, Ge (T) still turns out to be the dominant geometry (55%), the residue being made of defect O Ge sites that are either fourfold or fivefold coordinated. The dominant T character of Ge in the amorphous phase of GST225 seems in agreement with a very recent  $^{119}\text{Sn}$  Mössbauer study [82] that confirms a conclusion drawn from x-ray absorption spec-

troscopy [71]. The population of Sb sites appears to switch from a PYR geometry that is typical of Group V sulfides or selenides to a defect O one, reminiscent of crystalline GST.

Taken together, the present numerical results reveal the complexity of the GST networks that contain geometries which are highly sensitive to composition, thermodynamic conditions, and sample preparation. It is, for instance, now rather well established that the fraction of Ge-(T) depends crucially on the way the amorphous samples are generated [96,97]. In contrast to lighter chalcogenides such as

Ge-S, Ge-As-Se, or Ge-Sb-Se, where the elementary network building blocks can be regarded as stable T or PYR units, our investigation finally indicates that, for tellurides, atoms involved in local geometries experience larger bending motions which give rise to a variety of structural motifs. These arise from an increased delocalized bonding and/or metallicity which permit us to experience different types of local geometries and/or bonding. The presence of such “soft units” able to switch rather easily during the phase change mechanism appears to be generic.

- 
- [1] *Amorphous Chalcogenides: Structure, Properties, Modeling and Applications*, edited by A. V. Kolobov and K. Shimakawa (World Scientific, Singapore, City, 2020).
- [2] A. A. Piarristeguy, E. Barthélémy, M. Krbal, J. Frayret, C. Vigreux, and A. Pradel, *J. Non-Cryst. Solids* **355**, 2088 (2009).
- [3] S. Danto, P. Houizot, C. Boussard-Pledel, X. H. Zhang, F. Smektala, and J. Lucas, *Adv. Funct. Mat.* **16**, 1847 (2006).
- [4] K. Gunasekera, P. Boolchand, and M. Micoulaut, *J. Appl. Phys.* **115**, 164905 (2014).
- [5] B. J. Madhu, H. S. Jayanna, and S. Asokan, *Eur. Phys. J. B* **71**, 21 (2009).
- [6] K. Gunasekera, P. Boolchand, and M. Micoulaut, *J. Phys. Chem. B* **117**, 10027 (2013).
- [7] S. Bhosle, K. Gunasekera, P. Chen, P. Boolchand, M. Micoulaut, and C. Massabrio, *Solid St. Commun.* **151**, 1851 (2011).
- [8] T. Katsuyama and H. Matsumura, *J. Non-Cryst. Solids* **139**, 177 (1992).
- [9] S. Wei, G. J. Coleman, P. Lucas, and C. A. Angell, *Phys. Rev. Appl.* **7**, 034035 (2017).
- [10] P. Lebaudy, J. M. Saiter, J. Grenet, M. Belhadji, and C. Vautier, *Materials Sci. Eng. A* **132**, 273 (1991).
- [11] J. Akola and R. O. Jones, *Phys. Rev. Lett.* **100**, 205502 (2008).
- [12] S. Gabardi, S. Caravati, G. C. Sosso, J. Behler, and M. Bernasconi, *Phys. Rev. B* **92**, 054201 (2015).
- [13] A. Menelle, R. Bellissent, and A. M. Flank, *Europhys. Lett.* **4**, 705 (1987).
- [14] M. Micoulaut, K. Gunasekera, S. Ravindren, and P. Boolchand, *Phys. Rev. B* **90**, 094207 (2014).
- [15] P. S. Salmon, *J. Non-Cryst. Solids* **353**, 2959 (2007).
- [16] P. S. Salmon and A. Zeidler, *J. Stat. Mech.* (2019) 114006.
- [17] R. Azoulay, H. Thibierge, and A. Brenac, *J. Non-Cryst. Solids* **18**, 33 (1975).
- [18] J. M. Skelton, A. R. Pallipurath, T.-H. Lee, and S. R. Elliot, *Adv. Mater.* **24**, 7291 (2014).
- [19] W. Zhang, R. Mazzarello, M. Wuttig, and E. Ma, *Nat. Rev. Mat.* **4**, 150 (2019).
- [20] J. C. Phillips, *J. Non-Cryst. Solids* **34**, 153 (1979).
- [21] M. F. Thorpe, *J. Non-Cryst. Solids* **57**, 355 (1983).
- [22] H. He and M. F. Thorpe, *Phys. Rev. Lett.* **54**, 2107 (1985).
- [23] J. C. Maxwell, *Philos. Mag.* **27**, 294 (1864).
- [24] M. Micoulaut, *Adv. Physics X* **1**, 147 (2016).
- [25] *Phase Transitions and Self-organization in Electronic and Molecular Networks*, edited by M. F. Thorpe and J. C. Phillips (Kluwer Academic/Plenum, New York, 2001).
- [26] N. Mousseau and D. Drabold, *Eur. Phys. J. B* **17**, 667 (2000).
- [27] B. Effey and R. L. Cappelletti, *Phys. Rev. B* **59**, 4119 (1999).
- [28] P. Boolchand, D. G. Georgiev, and B. Goodman, *J. of Optoelectr. Adv. Mater* **3**, 703 (2001).
- [29] M. Micoulaut, *Phys. Rev. B* **74**, 184208 (2006).
- [30] J. Barré, A. R. Bishop, T. Lookman, and A. Saxena, *Phys. Rev. Lett.* **94**, 208701 (2005).
- [31] L. Yan and M. Wyart, *Phys. Rev. Lett.* **113**, 215504 (2014)
- [32] L. Yan, *Nature Comm.* **9**, 1359 (2018).
- [33] U. Vempati and P. Boolchand, *J. Phys. Condens. Matter* **16**, S5121 (2004)
- [34] S. Chakraborty and P. Boolchand, *J. Phys. Chem. B* **118**, 2249 (2014).
- [35] Q. Zhou, M. Wang, L. Guo, P. Boolchand, and M. Bauchy, *Front. Mater.* **6**, 157 (2019).
- [36] M. Bauchy and M. Micoulaut, *Nat. Comm.* **6**, 6398 (2015).
- [37] B. Mantis, M. Bauchy, and M. Micoulaut, *Phys. Rev. B* **92**, 134201 (2015).
- [38] W. Song, X. Li, M. Wang, M. Bauchy, and M. Micoulaut, *J. Chem. Phys.* **152**, 221101 (2020).
- [39] R. Chbeir, M. Bauchy, M. Micoulaut, and P. Boolchand, *Front. Mater.* **6**, 6 (2019).
- [40] M. Anbarasu and S. Asokan, *J. Phys. D* **40**, 7515 (2007).
- [41] A. Chaturvedi, G. S. Varma, G. Sreevidya, S. Asokan, and U. Ramamurty, *J. Non-Cryst. Solids* **543**, 120112 (2020).
- [42] G. S. Varma, C. Das, and S. Asokan, *Solid State Comm.* **177**, 108 (2014).
- [43] D. Roy, B. Tanujit, K. B. Jagannatha, G. S. Varma, S. Asokan, and C. Das, *J. Non-Cryst. Solids* **531**, 119863 (2020).
- [44] G. S. Varma, A. Chaturvedi, U. Ramamurty, and S. Asokan, *J. Non-Cryst. Solids* **471**, 251 (2017).
- [45] W. T. Laughlin and D. R. Uhlmann, *J. Phys. Chem.* **76**, 2317 (1972).
- [46] C. A. Angell, *Science* **267**, 1924 (1995).
- [47] M. Tatsumisago, B. L. Halfpap, J. L. Green, S. M. Lindsay, and C. A. Angell, *Phys. Rev. Lett.* **64**, 1549 (1990).
- [48] K. Gunasekera, S. Bhosle, P. Boolchand, and M. Micoulaut, *J. Chem. Phys.* **139**, 164511 (2013).
- [49] S. Ravindren, K. Gunasekera, Z. Tucker, A. Diebold, P. Boolchand, and M. Micoulaut, *J. Chem. Phys.* **140**, 134501 (2014).
- [50] S. Chakravarty, R. Chbeir, P. Chen, and M. Micoulaut, *Frontiers Mat.* **6**, 166 (2019).
- [51] A. Welton, R. Chbeir, M. McDonald, M. Burger, B. S. Almutairi, S. Chakravarty, and P. Boolchand, *J. Phys. Chem. C* **124**, 25087 (2020).
- [52] M. Micoulaut, *J. Phys. Condens. Matter* **22**, 285101 (2010).
- [53] H. Fores-Ruiz, G. G. Naumis, and M. Micoulaut, *J. Non-Cryst. Solids* **540**, 120127 (2020).



- [54] C. Yildirim, J.-Y. Raty, and M. Micoulaut, *Nature Comm.* **7**, 11086 (2016).
- [55] S. Chakravarty, B. Almutairi, R. Chbeir, S. Chakraborty, M. Bauchy, M. Micoulaut, and P. Boolchand, *Phys. Status Solidi B* **257**, 2000116 (2020).
- [56] K. Cheblia, J. M. Saiter, J. Grenet, A. Hamou, and G. Saffarini, *Physica B* **304**, 228 (2001).
- [57] J. Orava, L. Greer, B. Gholipour, D. W. Hewak, and C. E. Smith, *Nature Mat.* **11**, 279 (2012).
- [58] H. Flores-Ruiz and M. Micoulaut, *J. Chem. Phys.* **148**, 034502 (2018).
- [59] M. Micoulaut, *American Miner.* **93**, 1732 (2008)
- [60] D. Tonchev and S. O. Kasap, *J. Non-Cryst. Solids* **248**, 28 (1999).
- [61] M. Micoulaut, J.-Y. Raty, C. Otjacques, and C. Bichara, *Phys. Rev. B* **81**, 174206 (2010).
- [62] M. Micoulaut, M.-V. Coulet, A. Piarristeguy, M. R. Johnson, G. J. Cuello, C. Bichara, J.-Y. Raty, H. Flores-Ruiz, and A. Pradel, *Phys. Rev. B* **89**, 174205 (2014).
- [63] H. Flores-Ruiz, M. Micoulaut, M. V. Coulet, A. A. Piarristeguy, M. R. Johnson, G. J. Cuello, and A. Pradel, *Phys. Rev. B* **92**, 134205 (2015)
- [64] M. Micoulaut, A. Piarristeguy, H. Flores-Ruiz, and A. Pradel, *Phys. Rev. B* **96**, 184204 (2017)
- [65] M. Micoulaut and P. Boolchand, *Frontiers Mat.* **6**, 283 (2019).
- [66] J. Akola, R. O. Jones, S. Kohara, T. Usuki, and E. Bychkov, *Phys. Rev. B* **81**, 094202 (2010).
- [67] S. Grimme, *J. Comput. Chem.* **27**, 1787 (2006).
- [68] S. Kohara, K. Kato, S. Kimura, and H. Tanaka, *Appl. Phys. Lett.* **89**, 201910 (2006).
- [69] P. Jónvári, I. Kaban, J. Steiner, B. Beuneu, A. Schöps, and M. A. Webb, *Phys. Rev. B* **77**, 035202 (2008).
- [70] S. Howokawa, W.-C. Pilgrim, A. Höhle, S. Szubrin, N. Boudet, J.-F. Bérrar, and K. Maruyama, *J. Appl. Phys.* **111**, 083517 (2012).
- [71] A. Kolobov, P. Fons, A. I. Frenkel, A. L. Ankudinov, J. Tominaga, and T. Uruga, *Nature. Mat.* **3**, 703 (2004).
- [72] D. A. Baker, M. A. Paesler, G. Lucovsky, S. C. Agarwal, and P. C. Taylor, *Phys. Rev. Lett.* **96**, 255501 (2006).
- [73] P. Jónvári, I. Kaban, J. Steiner, B. Beuneu, A. Schöp, and A. Webb, *J. Phys. Cond. Matt.* **19**, 335212 (2007).
- [74] J. Akola and R. O. Jones, *Phys. Rev. B* **76**, 235201 (2007).
- [75] J. Akola, R. O. Jones, S. Kohara, S. Kimura, K. Kobayashi, M. Takata, T. Matsunaga, R. Kojima, and N. Yamada, *Phys. Rev. B* **80**, 020201(R) (2009).
- [76] J. R. Stellhorn, S. Hosokawa, and S. Kohara, *Analyt. Sci.* **36**, 5 (2020).
- [77] J. Akola and R. O. Jones, *Phys. Rev. B* **85**, 134103 (2012).
- [78] J. Akola and R. O. Jones, *J. Phys.: Condens. Matter* **20**, 465103 (2008).
- [79] S. Caravati, M. Bernasconi, T. D. Kühne, M. Krack, and M. Parrinello, *J. Phys. Condens. Matter* **21**, 255501 (2009).
- [80] M. Xu, Y. Q. Cheng, H. W. Sheng, and E. Ma, *Phys. Rev. Lett.* **103**, 195502 (2009).
- [81] M. Micoulaut, H. Flores-Ruiz, A. Pradel, A. Piarristeguy, *Physica Status Solidi RRL* **15**, 2000490 (2021).
- [82] A. V. Marchenko, E. I. Terukov, F. S. Nasredinov, and P. P. Seregin, *Tech. Phys. Lett.* **46**, 958 (2020).
- [83] P. Boolchand, *Physical Properties of Amorphous Materials*, edited by D. Adler, B. B. Schwartz, and M. C. Steele (Plenum Press, New York, 1985), pp. 221.
- [84] A. Piarristeguy, M. Micoulaut, R. Escalier, G. Silly, M.-V. Coulet, and A. Pradel, *J. Non-Cryst. Solids* **562**, 120730 (2021).
- [85] Z. Yang and P. Lucas, *J. Am. Ceram. Soc.* **92**, 2920 (2009).
- [86] C. N. Murthy, V. Ganesan, and S. Asokan, *Appl. Phys. A* **81**, 939 (2005).
- [87] A. Piarristeguy, A. Pradel, and J.-Y. Raty, *MRS Bull.* **42**, 45 (2017).
- [88] J. Luckas, A. Olk, P. Jost, H. Volker, J. Alvarez, A. Jaffré, P. Zalden, A. Piarristeguy, A. Pradel, C. Longeaud, and M. Wuttig, *Appl. Phys. Lett.* **105**, 092108 (2014).
- [89] M. Bauchy, A. Kachmar, and M. Micoulaut, *J. Chem. Phys.* **141**, 194506 (2014).
- [90] S. Chakraborty, P. Boolchand, and M. Micoulaut, *Phys. Rev. B* **96**, 094205 (2017).
- [91] V. B. Rao, C. F. George, S. Wolff, and W. C. Agosta, *J. Am. Chem. Soc.* **107**, 5732 (1985).
- [92] R. Keese, *Chem. Rev.* **106**, 4787 (2006).
- [93] S. Caravati, M. Bernasconi, T. D. Kühne, M. Krack, and M. Parrinello, *Appl. Phys. Lett.* **91**, 171906 (2007).
- [94] J.-Y. Raty, C. Otjacques, J. P. Gaspard, and C. Bichara, *Solid State Sci.* **12**, 193 (2010).
- [95] E. Lascaris, M. Hemmati, S. V. Buldyrev, H. E. Stanley, and C. A. Angell, *J. Chem. Phys.* **140**, 224502 (2014).
- [96] P. K. Khulbe, E. M. Wright, and M. Mansipur, *J. Appl. Phys.* **88**, 3926 (2000).
- [97] J. Akola, J. Larrucea, and R. O. Jones, *Phys. Rev. B* **83**, 094113 (2011).